Nanoscale capillary freezing of ionic liquids confined between metallic interfaces and the role of electronic screening

Jean Comtet[1], Antoine Niguès[1], Vojtech Kaiser[1], Benoit Coasne[2], Lydéric Bocquet[1] and Alessandro Siria[1]*

Room-temperature ionic liquids (RTILs) are new materials with fundamental importance for energy storage and active lubrication. They are unusual liquids, which challenge the classical frameworks of electrolytes, whose behaviour at electrified interfaces remains elusive, with exotic responses relevant to their electrochemical activity. Using tuning-fork-based atomic force microscope nanorheological measurements, we explore here the properties of confined RTILs, unveiling a dramatic change of the RTIL towards a solid-like phase below a threshold thickness, pointing to capillary freezing in confinement. This threshold is related to the metallic nature of the confining materials, with more metallic surfaces facilitating freezing. This behaviour is interpreted in terms of the shift of the freezing transition, taking into account the influence of the electronic screening on RTIL wetting of the confining surfaces. Our findings provide fresh views on the properties of confined RTIL with implications for their properties inside nanoporous metallic structures, and suggests applications to tune nanoscale lubrication with phase-changing RTILs, by varying the nature and patterning of the substrate, and application of active polarization.

The confinement of liquids at nanoscales leads to a broad spectrum of new properties which can be harnessed in a variety of applications, from energy storage and friction to catalysis[1–6]. The nanoscale realm indeed hosts a broad spectrum of molecular forces that compete to make new fluid behaviour emerge[7–10] via the interaction of the liquid with the confining interfaces.

In this work, we explore the mechanical behaviour of room-temperature ionic liquids (RTILs) in nanoscale confinement. Such system is a prototype for a dense electrolyte—composed here of pure ions—and, accordingly, electrostatic interactions do control the behaviour of these liquids. However, the absence of solvent in RTILs leads to strong electrostatic coupling between ions and to the breakdown of standard mean-field response, which constitutes the toolbox of dilute electrolytes. Moreover, the behaviour of RTILs at interfaces remains elusive, with rich and peculiar behaviours[11–22].

Confinement therefore opens an interesting window on the physics of dense electrolytes and their interaction with the confining interfaces[23–25]. In particular, due to the dominant role of electrostatic forces, one may anticipate that the metallic nature of the confining surfaces should affect the static and dynamic properties of confined RTILs. Such a relationship has not been experimentally explored up to now.

Experimental set-up

We present in Fig. 1a a sketch of the experimental set-up (see Supplementary Information 1 for more details). Briefly, we glue an electrochemically etched tungsten tip of end radius from 50 nm to 2.5 μm to a millimetric quartz tuning fork, which serves as our force sensor. The tuning fork is excited via a piezo dither, and the oscillation amplitude and phase shift of the tuning fork with regards to the excitation voltage are monitored via the piezoelectric current flowing through the tuning fork electrodes. By means of a piezo-element with sub-nanometric resolution in displacement, the probed liquid is confined between the oscillating tungsten tip and substrates of various nature. Importantly, the entire set-up is placed in a vacuum chamber at a pressure of approximately 10^{-5} mbar.

This set-up allows us to measure the mechanical impedance $Z^* = F^*/h_0 = Z' + iZ''$ [N m^{-1}] of the confined liquid, defined as the ratio of the complex amplitude of the dynamic force F^* [N] acting on the tip, to the amplitude h_0 [m] of the tip oscillation. The inset of Fig. 1b shows a typical resonance curve of the tuning fork for a fixed excitation voltage of the piezoelectric element, with the tip immersed in a Newtonian silicone oil far from the surface (1), close to the surface (2) and in contact with the substrate (3). As the interaction of the tip with its environment is modified, one observes a change in both the resonance frequency and the amplitude at resonance. The shift in resonance frequency δf [Hz] is related to the conservative force response Z', whereas the broadening of the resonance (change of quality factor $Q_0 \rightarrow Q_1$) is related to dissipation Z'' (ref. 26). During a typical experiment, two feedback loops allow us to work at the resonance and maintain constant the oscillation amplitude h_0 of the tuning fork. Monitoring the frequency shift δf and the excitation voltage V_i [V] thus provides a direct measurement of the real ($Z' = \text{Re}(Z^*)$) and imaginary ($Z'' = \text{Im}(Z^*)$) parts of the mechanical impedance.

The experimental set-up has been fully benchmarked using a Newtonian silicone oil, as shown in Fig. 1b. Experimentally Z^* is extracted from the frequency shift δf and the change in the quality factor at the resonance ($Q_0 \rightarrow Q_1$):

$$Z' = 2K_0 \frac{\delta f}{f_0} \text{ and } Z'' = K_0 \left(\frac{1}{Q_0} - \frac{1}{Q_1} \right) \quad (1)$$

[1]Laboratoire de Physique Statistique, Ecole Normale Supérieure, UMR CNRS 8550, PSL Research University, 75005 Paris Cedex 05, France. [2]Laboratoire Interdisciplinaire de Physique, CNRS and Université Grenoble Alpes, UMR CNRS 5588, 38000 Grenoble, France. *e-mail: alessandro.siria@lps.ens.fr
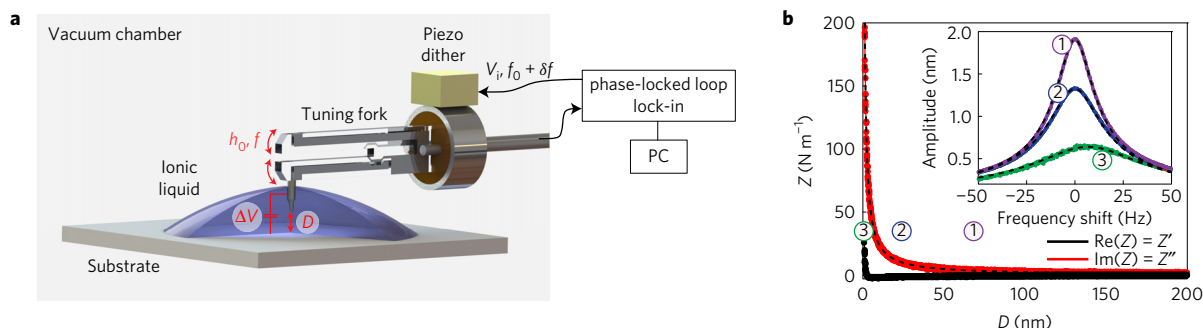
Figure 1 | Experimental set-up. a, Schematic of the experiment. An etched tungsten tip of end radius of curvature R between 50 nm and 2.5 μm is glued to the tuning fork, and immersed in the RTIL. The tuning fork is excited by a piezo dither at a frequency $f_0 \approx 32$ kHz, and a lock-in and a phase-locked loop maintain constant both the oscillation amplitude h_0 and the phase shift between the tuning fork and the excitator. The distance D between the tip and the substrate is controlled through a piezo-element with sub-nanometric resolution in displacement. The substrate can be biased with respect to the tip by a potential difference ΔV. The experimental set-up is placed in a vacuum chamber at a pressure of $\approx 10^{-5}$ mbar. **b**, Nanorheological measurement on a silicone oil confined between a tungsten tip and a mica sample, showing the variation of conservative (Z', black) and dissipative (Z'', red) mechanical impedance (see equation (1)); black dotted line is a fit based on equation (2). Inset shows typical resonance curves of the tuning fork with the tip immersed in the liquid and far from the surface (1), close to the surface (2) and in contact with the substrate (3).

where f_0 [Hz] is the bare resonance frequency and K_0 [N m^{-1}] is the tuning fork spring constant. The advantages of the tuning fork are twofold: first, an ultrahigh stiffness of $K_0 \approx 40$ kN m^{-1}, which prevents any mechanical instability during the approach, and second, very low oscillation amplitude h_0 (0.1–2 nm) together with very low intrinsic dissipation, characterized by high quality factors of up to tens of thousands in vacuum and in the range of few thousands even when the tip is immersed in high-viscosity liquid. These characteristics make the tuning fork atomic force microscope (AFM) the ideal instrument to study, for example, tribology in individual nanostructures such as nanowires and nanotubes[26].

The RTIL under investigation is [Bmim][BF4] (Sigma Aldrich, 98.5% purity), which is further filtered through a 100 nm hole Teflon membrane before use. A drop is deposited on the substrate and the AFM tungsten tip is immersed in the liquid. The liquid is left at rest in the vacuum chamber for at least 12 h to remove water impurities. The substrate can be biased with respect to the tip by a potential difference ΔV. To verify the high purity of the ionic liquid, we systematically check the absence of a long-term electrochemical current when applying a potential drop between -1.8 V and 1.8 V, which is smaller than the electrochemical window for this liquid[27].

We have explored various substrates, namely mica, highly oriented pyrolytic graphite (HOPG), doped silicon, and platinum, whose characteristics are described in Supplementary Information 2. Note that platinum and doped silicon may be coated by natural oxide layers of up to 1 nm in thickness[28,29], but we anticipate from our results below that this value is much smaller than the typical length at which the phenomena under investigation occur, in the range of tens of nanometres.

Confinement-induced freezing

We plot in Fig. 2a the typical variation of the elastic $Z' = \text{Re}(Z^*)$ (black curve) and dissipative $Z'' = \text{Im}(Z^*)$ (red curve) parts of the mechanical impedance, as the tungsten tip approaches a HOPG surface in the ionic liquid. Far from the substrate—zone (i)—the elastic response $Z' \approx 0$ within experimental precision; one can observe a minute attractive component reminiscent of what is observed in refs 30,31. The dissipative component Z'' increases gently as the confinement thickness decreases; quantitatively, the increase of Z'' with decreasing confinement D can be described by the Reynolds dissipative response of a viscous Newtonian fluid sheared by an oscillating sphere[32]:

$$Z^*(D) = i\frac{6\pi\eta R^2 2\pi f_0}{D} \qquad (2)$$

where $R \approx 1$–2.5 μm is the radius of curvature of the tip, $\eta \approx 0.15$ Pa s the liquid bulk viscosity, $f_0 \approx 32$ kHz the oscillation frequency and D [nm] the distance between the tip and the substrate. This expression assumes no slip at the liquid/substrate interfaces, which is expected for strongly interacting systems like ionic liquids[7]. To avoid errors induced by the real geometry of the tungsten tip (see Supplementary Information, Fig. S1) we calibrated the technique on a silicone oil with viscosity $\eta \approx 0.1$ Pa s, comparable to $\eta \approx 0.15$ Pa s for our RTIL. As shown in Figs 1c and 2a, this prediction reproduces very well the experimental data and allows one to determine the 'hydrodynamic zero', which defines the absolute distance D between the tip and the substrate (see Supplementary Information 1).

As shown in Fig. 2a, in ionic liquids, before reaching the hydro-dynamic 'zero' $D \rightarrow 0$, both the elastic Z' and dissipative part Z'' of the response suddenly diverge at a critical confinement $D = \lambda_S$. This occurs for confinements D in the range of a few tens of nanometres, depending on the substrate. We have changed the tip oscillation amplitude h_0 over one decade, between 0.1 nm and 1 nm, to verify that λ_S does not depend on the oscillation amplitude and shear rates.

This strong repulsive elastic response (with $Z' \approx 10$ N m^{-1}) shows that the ionic liquid can now sustain a yield stress of order $\tau \approx Z'h_0/\pi R^2 \approx 1$ kPa, providing a clear signature of the solid-like response of the confined RTIL for $D < \lambda_S$. This behaviour was found repeatedly when performing approach and retract cycles of the tip, either at the same or at distinct locations; typically 10,000 cycles were performed for each material, over 20 distinct locations. We measured accordingly the distribution of threshold confinement thickness, as reported in the inset of Fig. 2b for HOPG, allowing us to extract the mean transition thickness, found to be $\lambda_S \simeq 60$ nm for HOPG.

Going further, the same phenomenon was observed for the various substrates under investigation: mica, HOPG, doped silicon and platinum, with a mean transition thickness λ_S increasing in the order: mica (15 nm) < HOPG (60 nm) < doped silicon (110 nm) < platinum (160 nm). Interestingly this order corresponds to substrates with increasing metallic character, as for example characterized by the conductivity, from the insulating mica to the highly conductive platinum.

Prewetting, capillary freezing and electronic screening

As a first interpretation of these results, one may infer the presence of solid layers pre-existing on the surface of the substrates. To explore this assumption, we have acquired AFM images of the surfaces using a sharp tip with a 10–50 nm of radius of curvature. While in vacuum, the substrates surface appear atomically smooth
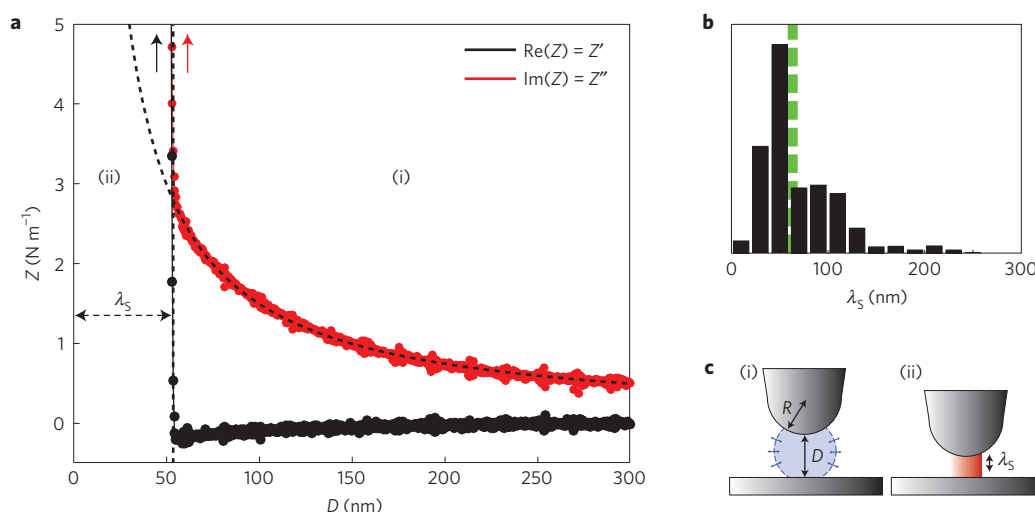
Figure 2 | Confinement-induced freezing transition. a, Typical approach curve on a HOPG substrate. Real (Z', black) and complex (Z'', red) part of the mechanical impedance, characterizing the conservative and dissipative response of the liquid, versus tip–substrate position D, performed on a HOPG sample. The origin of the tip–substrate position is defined as the hydrodynamic zero obtained by fitting Z'' with equation (2). Upon a critical confinement distance λ_S, Z changes from a liquid-like response to a solid-like response, characterized by the onset of an elastic contribution (Z', black dots) and a sharp increase of the dissipation (Z'', red dots), as Z' and Z'' diverge to values up to 10 N m^{-1}. **b**, Distribution of λ_S on HOPG; $\approx$12,000 cycles were performed, over 18 distinct locations. Green vertical line is the mean of the distribution. **c**, Sketch of the freezing induced by confinement: upon a critical confinement the RTIL changes from liquid (i) to solid-like (ii).

on micrometric scales—with a typical r.m.s. roughness between 0.3 nm and 1 nm depending on the substrate, see Supplementary Information, Fig. S2—one indeed observes solid-like terrace structures on the surfaces when immersed in RTIL. This thickness is measured below 1 nm for HOPG and typically in the range of ~20–30 nm for doped silicon and platinum; no such terrace is evident on mica, see Supplementary Information, Fig. S3. Such structures are reminiscent of previous observations using scanning tunnelling microscopy and AFM imaging[16,21,33,34].

That such thick structures are present on the substrate surfaces is unexpected *per se* and raises the question of the prewetting of the surfaces by the RTIL, and the role of the metallic nature of the substrates on this prewetting. We note, however, that the characteristic height of these solid 'prewetting' films is much smaller than the critical thickness at which the solidification transition (Fig. 2a) occurs for each substrate (Fig. 3, blue dots). Accordingly an alternative thermodynamic explanation should be sought.

Looking at Fig. 2a, the drastic change in both elastic response and dissipation from $D > \lambda_S$ to $D < \lambda_S$ would actually rather suggest a complete confinement-induced phase change, with a freezing of the confined RTIL inside the gap. Such a confinement-induced phase transition is expected when surface energies stabilize the unfavoured (solid) phase by compensating for the bulk free energy of freezing. This results in a shift for the phase transition, as observed for capillary condensation (the shifted liquid–gas phase transition) or capillary freezing (shifted crystallization)[35]. The balance of free energy leads to the so-called Gibbs–Thomson equation, which characterizes the critical confinement λ_S at which the free energies of the liquid and solid phase become equal[35]:

$$\Delta T = T_C - T_B = 2 \frac{T_B \Delta\gamma}{\rho L_h \lambda_S} \text{ with } \Delta\gamma = \gamma_{wl} - \gamma_{ws} \quad (3)$$

where $\Delta T = T_C - T_B$ is the shift in transition temperature, in confinement T_C as compared to the bulk transition occurring at T_B. For the specific ionic liquid used here, $T_B = -71\,°C$; γ_{wl} and γ_{ws} are the surface energy of the liquid and solid phase with respect to the wall/substrate, $\rho = 1.21\,g\,ml^{-1}$ the density of the liquid phase and $L_h = 47\,kJ\,kg^{-1}$ the latent heat of melting[36] (see Supplementary Table 1). Equation (3) shows that if wetting of the solid phase

on the substrate is favoured compared to that of the liquid ($\gamma_{ws} < \gamma_{wl}$) then the freezing temperature of the confined phase T_C is higher than the bulk freezing temperature T_B ($T_C > T_B$ in equation (3)). Putting in numbers, one gets $T_C \sim 25\,°C$ for a RTIL confined in a gap of ~20 nm with $\Delta\gamma \sim 0.3\,J\,m^{-2}$ (anticipating the values below). In other words, the RTIL may freeze in nanoconfinement at room temperature. In this scenario, the distribution of confinement length measured experimentally (Fig. 2b) can be understood as a signature of activation due to the first-order character of the freezing transition (potentially facilitated by the prewetting phase on the substrate). To get a first hint on the behaviour of such systems, we have validated this scenario and the Gibbs–Thomson relationship on the basis of molecular dynamics simulations of a model ionic systems in confinement (see Supplementary Information 6).

A delicate question, however, is to understand the variations with the metallic nature of the substrate. Following the argument above in terms of the shifted liquid–solid transition, this raises the question of the crystal–substrate surface energy and how it is influenced by the metallic character of the substrate. Physically, one may propose a simple explanation in terms of image charges. To highlight the argument, let us consider a semi-infinite ionic crystal at the interface with a perfect metal, as sketched in Fig. 3c (Fig. 3b shows an imperfect metal). The network of image charges builds a crystal structure with a (nearly) perfect symmetry with respect to the real half-lattice (right-hand side). Accordingly one expects the electrostatic contribution to the surface free energy to (nearly) vanish, as the system behaves as a single bulk lattice: $\gamma_{ws}^{elec} \to 0$. This, of course, requires a perfectly symmetric crystalline structure (Fig. 3c), and this cancellation is not expected to occur for insulating substrates (Fig. 3b) or for disordered liquid phases. In other words, the (semi-infinite) ionic crystal has a lower surface energy at the interface with a metal wall as compared to an insulating substrate: $\gamma_{ws}^{insulating} > \gamma_{ws}^{metal}$. This shows that the crystal phase is favoured on a metallic surface as compared to an insulating surface and the Gibbs–Thomson equation (3) accordingly implies that the threshold confinement for the freezing transition should be larger with metal as compared to insulating confining surfaces. Going beyond requires one to get further predictions for the surface effects at metallic walls which enter the Gibbs–Thomson equation, equation (3).
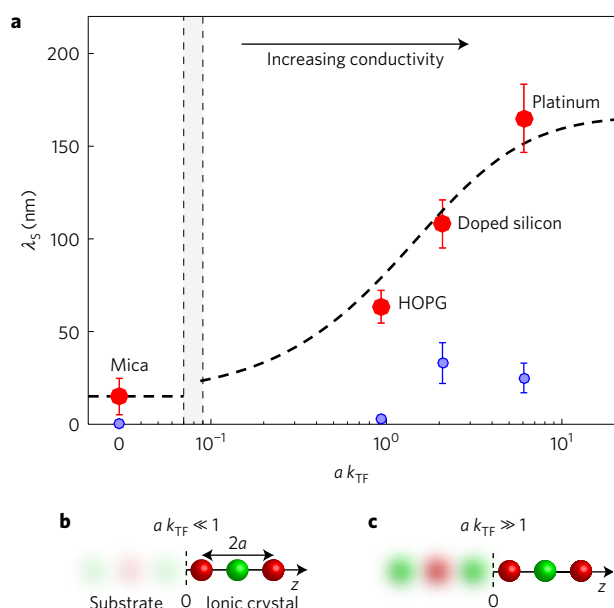
Figure 3 | Effect of substrate electronic properties on the freezing transition. a, Red dots: Variation of the mean solidification length λ_S on mica and three conductive substrates: HOPG, doped silicon and platinum versus the normalized Thomas–Fermi wavevector, $a\,k_{TF}$, with $2a$ the typical ionic crystal lattice constant. Error bars indicate standard deviation for mica and standard error for the three conductive substrates, with $N \approx 20$ the number of positions investigated in each substrate. Blue open dots represent the typical size of the pre-existing solid layers measured with a sharp tip. Error bars represent standard deviation of the estimated height. Dotted line is the prediction from equation (7). **b,c**, Schematic representation of the ionic crystal close to an insulator ($a\,k_{TF} \ll 1$, (**b**)) and a perfect metal ($a\,k_{TF} \gg 1$, (**c**)) for which image charges induced in the substrate decrease the energy of the system.

To account for the non-ideal metallic nature of the confining walls, one should model the electronic screening inside the substrates. To this end, we use the simple Thomas–Fermi framework, based on a local density approximation for the free electron gas[37]. This description provides a simple screening equation for the electric potential V (V) [V] in the metal, where the screening length $\lambda_{TF} = 1/k_{TF}$ [m] characterizes the typical length over which a defect charge is screened in the metal and is defined in terms of the density of states at the Fermi level, according to $k_{TF}^2 = 4\pi e^2 (\partial n/\partial \epsilon_F)$; n the state occupation and ϵ_F the Fermi level. The limit of large k_{TF} (small λ_{TF}) corresponds to the perfect metallic case, for which V is uniformly zero. The electronic screening therefore modifies the interactions of charge close to the liquid–wall interface and the Green function Ψ for the electrostatic interaction, replacing the Coulomb interaction, obeys the equations:

$$\Delta \psi = -\frac{Q}{\epsilon}\delta(\mathbf{r} - \mathbf{r}_0) \quad \text{for } z > 0$$

$$\Delta \psi - k_{TF}^2 \psi_{TF} = 0 \quad \text{for } z < 0 \qquad (4)$$

where ϵ [F m^{-1}] is the ionic crystal dielectric constant.

This allows us to calculate the energy of a semi-infinite ionic system in the presence of the metallic walls, as $U = (1/2)\int \mathbf{dr}\rho_c(\mathbf{r})\psi(\mathbf{r})$, with ρ_c the charge density. For the crystal phase $\rho_{cr}(\mathbf{r}) = Q\sum_n(-1)^n \delta(\mathbf{r} - \mathbf{R_n})$, with R_n the lattice sites, while for the liquid phase, the charge density $\rho_{liq}(\mathbf{r})$ vanishes beyond a few molecular layers close to the wall. The calculation of this energy is a very challenging task, because both the one-body interaction of ions with their image charges, and the two-body interactions

between ions, are strongly modified by the presence of the confining metallic (TF) wall. In the present work, we develop a simplifying description which captures the main effects of wall metallicity on the surface electrostatic energies, with the objective to rationalize the experimental data. This framework is described in Supplementary Information 5. Overall, we predict that the surface tension excess, of the ionic liquid–metal versus the ionic crystal–metal interfaces, is a function of the TF screening parameter k_{TF}, taking the form

$$\Delta\gamma = \gamma_{WL} - \gamma_{WC} \approx \Delta\gamma^{ins} + \frac{Q^2 \Delta\rho}{16\pi\epsilon} \times \mathcal{F}(k_{TF}a) \qquad (5)$$

where $\Delta\gamma^{ins} = \gamma_{WL}^{ins} - \gamma_{WC}^{ins}$ [J m^{-2}] is the difference in surface energies at insulating walls, $\Delta\rho = \rho_C - \rho_L$ (m^{-3}) is the density difference between the ionic crystal and ionic liquid phases ($\Delta\rho > 0$), a [m] is an ionic molecular size (typically given by the ionic crystal lattice constant), and $Q = e$ [C] is the elementary ionic charge. The dimensionless function $\mathcal{F}$, whose expression is given in Supplementary Information Equation (10), is an increasing function of TF screening k_{TF}; it interpolates between 0 and 1 with a crossover occurring for $k_{TF}a \sim 1$. As a guideline, it can be well approximated as $\mathcal{F}(x) \approx x/(\nu + x)$ with $\nu \simeq 1.7$ (see Supplementary Information). The steps leading to this expression are discussed in details in Supplementary Information 5. Overall, the physical picture underlying equation (5) is that the electrostatic contribution to the surface energy—in excess to the insulating wall situation—originates merely from the direct interaction of ions close to the surface with their image charge, the latter being modified by the TF screening. Interestingly, this approximated approach emerges from exact calculations for the one-dimensional crystal–wall interface, which capture the main ingredients at stake and allow us to calculate analytically the surface energy for any TF screening parameter k_{TF}. These calculations validate the simplified estimate of the excess surface energy in terms of image charge interactions for a dense ionic system at the interface with a metallic wall, which is then extended to the liquid–wall interface. As a complementary check of the framework, molecular simulations of a model ionic system at finite temperature confirm the lower energy of the crystal–wall interface as compared to the liquid–wall interface in the case of an insulating confining substrate, as well as the order of magnitude of the various contributions to the surface energies (see Supplementary Information 6). Altogether we obtain $\Delta\gamma^{ins} = \Delta\gamma^0 (1 + \delta\mathcal{F}(k_{TF}a))$, where $\Delta\gamma^0$ [J m^{-2}] is the surface tension difference between of the liquid–wall versus crystal–wall interfaces for an insulating substrate and including also the non-electrostatic contributions to the surface energy (van der Waals, and so on) and the possible (constant) contribution from the tungsten tip. The dimensionless parameter $\delta = e^2(\rho_C - \rho_L)/(16\pi\epsilon\,\Delta\gamma_0)$ quantifies the contribution of metallicity to the surface energies.

Now using the Gibbs–Thomson result, equation (3), one predicts that the increase in surface energy difference for better metals—that is, for a larger Thomas–Fermi wavevector k_{TF} (equation (5)) will lead to a shift in the critical confinement distance for the freezing transition according to

$$\lambda_S = \lambda_S^0 (1 + \delta \cdot \mathcal{F}(k_{TF}a)) \qquad (6)$$

with λ_S^0 the value for the perfectly insulating material defined in terms of $\Delta\gamma_0$ (here for the mica substrate).

In Fig. 3, we compare the prediction for λ_S with the experimental data for the various substrates investigated. Note that, in doing this comparison, we estimated the values of Thomas–Fermi length based on the substrate conductivity and carrier density (see Supplementary Information 2). We also fixed the molecular length to the crystal lattice constant as $2a = 0.67$ nm (as estimated from the molar volume of the RTIL). As shown in Fig. 3, a good agreement
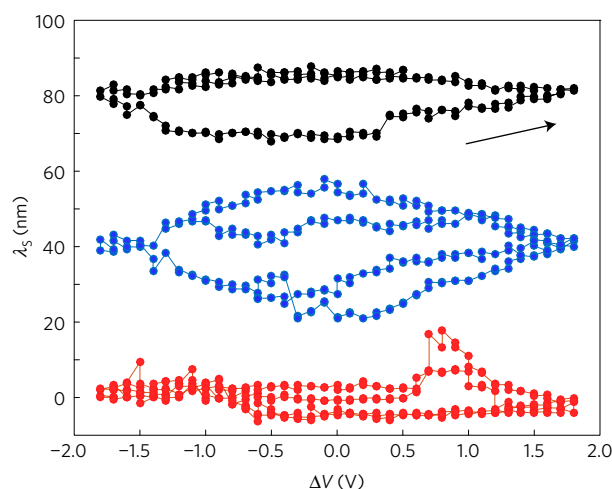
Figure 4 | Voltage-induced freezing. Hysteresis cycle in the solidification length λ_S versus tip–sample bias ΔV (V) for HOPG (red), doped silicon (blue) and platinum (black). Arrow indicates cycle direction. The absolute cycle position is shifted for clarity. Mean absolute cycle position is $\langle \lambda_S \rangle = 45$ nm for HOPG, $\langle \lambda_S \rangle = 85$ nm for silicon and $\langle \lambda_S \rangle = 150$ nm for platinum.

between the theoretical predictions and the experimental results is obtained, yielding $\lambda_S^0 = 15$ nm and $\delta = 10.1$. From the value for λ_0 and equation (3), one gets $\Delta\gamma_0 \approx 0.2\,\mathrm{J\,m^{-2}}$. Using equation (6), and assuming $\rho_L/\rho_C \sim 0.8$ as typical for such systems[38], this would predict a value of $\delta \approx 10^0$, in fair agreement with the value obtained from the fit of the experimental data, $\delta \approx 10$.

Finally, we might also expect the bias voltage ΔV applied between the two confining substrates to affect surface energies and tune the freezing transition. While measuring the critical confinement distance λ_S for each applied voltage ΔV, we could indeed observe hysteresis cycles in the critical confinement length, with a peak-to-peak amplitude of approximately 20 nm (Fig. 4). Following equation (3), we can interpret the dependence of the critical confinement length λ_S on the bias voltage ΔV by considering the additional contributions to surface energies due to the charged capacitance at the substrate/ionic liquid interface as:

$$\Delta\gamma = \tilde{\Delta}\gamma + \frac{1}{2} C \cdot \Delta V^2 \qquad (7)$$

where the last term is the area energy density stored in the capacitor, with C the interfacial capacitance per surface area, and $\tilde{\Delta}\gamma$ takes into account all of the other electronic and non-electronic contributions to surface energies. Considering a typical capacitance of the order of $0.1\,\mathrm{F\,m^{-2}}$ (ref. 39), we obtain an additional surface energy of $0.2\,\mathrm{J\,m^{-2}}$, leading to a predicted cycle amplitude of 15 nm, in very good agreement with our experimental results. Those results suggest voltage-induced controls of ionic liquid materials, as experienced in previous experiments[40,41] and theoretical work[42,43].

Discussion

The agreement between the experimental data (Figs 3 and 4) and the predictions supports the proposed picture of a shifted freezing transition, with wetting properties tuned by the electronic screening inside the confining substrates and the bias voltage between the confining substrates. There is room for improvement of the theory, with a more complete description of the effect of the electronic screening on the RTIL wetting. This theoretical framework, which has not been developed up to now, will be the subject of future work.

Our results also have implications for the question of dynamics of charging in dense electrolytes confined between metal surfaces, which is relevant to supercapacitor dynamics[12]. Despite the

importance of these phenomena for further development of supercapacitors, there is so far a lack of experimental studies at the nanoscale, while unexpected phenomena were predicted at these scale[44]. Our work underlines that the nanoscale is a peculiar lengthscale for ionic liquids, and leads to strongly different behaviour from what is observed in the bulk. Our measurements unveil an overlooked phenomenon, suggesting that further improvements of the performance can be sought at the scales dominated by the atomic nature of matter. Other exotic behaviours might emerge for confinements of the order of the ion size[44–46], while the presence of disordered and rough surfaces, as typically present in supercapacitors might prevent the freezing transition reported here[12]. Further experimental and theoretical investigations of these regimes seem now to be necessary in light of our study.

In the context of lubrication, our results also suggest to take advantage of the dramatic and abrupt RTIL phase change to tune nanoscale friction via modifications of the substrate, from insulating to metallic, and possibly with dedicated patterning via metallic coating. The relatively weak solid phase would indeed prevent (un-desired) direct substrate–substrate contact by generating normal forces. The solid phase could be regenerated in situ, as it takes its origin in the RTIL confinement. Furthermore, the modification of the confinement-induced transition under a voltage drop could finely modify the lubricating state by active polarization. While such perspectives require further exploration, they open new and exciting perspectives for phase-changing lubricants.

References

1. Armand, M., Endres, F., MacFarlane, D. R., Ohno, H. & Scrosati, B. Ionic-liquid materials for the electrochemical challenges of the future. *Nat. Mater.* **8,** 621–629 (2009).
2. Uesugi, E., Goto, H., Eguchi, R., Fujiwara, A. & Kubozono, Y. Electric double-layer capacitance between an ionic liquid and few-layer graphene. *Sci. Rep.* **3,** 1595 (2013).
3. Palacio, M. & Bhushan, B. A review of ionic liquids for green molecular lubrication in nanotechnology. *Tribol. Lett.* **40,** 247–268 (2010).
4. Dold, C., Amann, T. & Kailer, A. Influence of electric potentials on friction of sliding contacts lubricated by an ionic liquid. *Phys. Chem. Chem. Phys.* **17,** 10339–10342 (2015).
5. Smith, A. M., Lovelock, K. R. J., Gosvami, N. N., Welton, T. & Perkin, S. Quantized friction across ionic liquid thin films. *Phys. Chem. Chem. Phys.* **15,** 15317–15320 (2013).
6. Siria, A. *et al.* Giant osmotic energy conversion measured in a single transmembrane boron nitride nanotube. *Nature* **494,** 455–458 (2013).
7. Bocquet, L. & Charlaix, E. Nanofluidics, from bulk to interfaces. *Chem. Soc. Rev.* **39,** 1073–1095 (2010).
8. Secchi, E., Niguès, A., Jubin, L., Siria, A. & Bocquet, L. Scaling behavior for ionic transport and its fluctuations in individual carbon nanotubes. *Phys. Rev. Lett.* **116,** 154501 (2016).
9. Secchi, E. *et al.* Massive radius-dependent flow slippage in single carbon nanotubes. *Nature* **537,** 210–213 (2016).
10. Agrawal, K. V., Shimizu, S., Drahushuk, L. W., Kilcoyne, D. & Strano, M. S. Observation of extreme phase transition temperatures of water confined inside isolated carbon nanotubes. *Nat. Nanotech.* **12,** 267–273 (2017).
11. Fedorov, M. V. & Kornyshev, A. A. Ionic liquids at electrified interfaces. *Chem. Rev.* **114,** 2978–3036 (2014).
12. Merlet, C. *et al.* On the molecular origin of supercapacitance in nanoporous carbon electrodes. *Nat. Mater.* **11,** 306–310 (2012).
13. Perkin, S., Salanne, M., Madden, P. & Lynden-Bell, R. Is a Stern and diffuse layer model appropriate to ionic liquids at surfaces? *Proc. Natl Acad. Sci. USA* **110,** E4121 (2013).
14. Atkin, R. *et al.* AFM and STM studies on the surface interaction of [BMP]TFSA and (EMIm)TFSA ionic liquids with Au(111). *J. Phys. Chem. C* **113,** 13266–13272 (2009).

15. Rotenberg, B. & Salanne, M. Structural transitions at ionic liquids interfaces. *J. Phys. Chem. Lett.* **6,** 4978–4985 (2015).
16. Endres, F., Borisenko, N., El Abedin, S. Z., Hayes, R. & Atkin, R. The interface ionic liquid(s)/electrode(s): *in situ* STM and AFM measurements. *Faraday Discuss.* **154,** 221–233 (2012).
17. Borisenko, N., Atkin, R., Lahiri, A., El Abedin, S. Z. & Endres, F. Effect of dissolved LiCl on the ionic liquid-Au(111) interface: an *in situ* STM study. *J. Phys. Condens.* **26,** 284111 (2014).
18. Liu, Y., Zhang, Y., Wu, G. & Hu, J. Coexistence of liquid and solid phases of Bmim-PF6 ionic liquid on mica surfaces at room temperature. *J. Am. Chem. Soc.* **128,** 7456–7457 (2006).
19. Bovio, S., Podestà, A., Milani, P., Ballone, P. & Del Pópolo, M. G. Nanometric ionic-liquid films on silica: a joint experimental and computational study. *J. Phys. Condens. Matter* **21,** 424118 (2009).
20. Bovio, S., Podesta, A., Lenardi, C. & Milani, P. Evidence of extended solidlike layering in [Bmim][NTf2] ionic liquid thin films at room-temperature. *J. Phys. Chem. B* **113,** 6600–6603 (2009).
21. Yokota, Y., Harada, T. & Fukui, K. I. Direct observation of layered structures at ionic liquid/solid interfaces by using frequency-modulation atomic force microscopy. *Chem. Commun.* **46,** 8627–8629 (2010).
22. Lee, A. A. & Perkin, S. Ion-image interactions and phase-transition at electrolyte-metal interface. *J. Phys. Chem. Lett.* **7,** 2753–2757 (2016).
23. Ueno, K., Kasuya, M., Watanabe, M., Mizukami, M. & Kurihara, K. Resonance shear measurement of nanoconfined ionic liquids. *Phys. Chem. Chem. Phys.* **12,** 4066–4071 (2010).
24. Jurado, L. A. *et al.* Irreversible structural change of a dry ionic liquid under nanoconfinement. *Phys. Chem. Chem. Phys.* **17,** 13613–13624 (2015).
25. Bou-Malham, I. & Bureau, L. Nanoconfined ionic liquids: effect of surface charges on flow and molecular layering. *Soft Matter* **6,** 4062–4065 (2010).
26. Niguès, A., Siria, A., Vincent, P., Poncharal, P. & Bocquet, L. Ultra-high interlayer friction inside boron-nitride nanotubes. *Nat. Mater.* **13,** 688–693 (2014).
27. O'Mahony, A. M., Silvester, D. S., Aldous, L., Hardacre, C. & Compton, R. G. Effect of water on the electrochemical window and potential limits of room-temperature ionic liquids. *J. Chem. Eng. Data* **53,** 2884–2891 (2008).
28. Morita, M., Ohmi, T., Hasegawa, E., Kawakami, M. & Ohwada, M. Growth of native oxide on a silicon surface. *J. Appl. Phys.* **68,** 1272–1281 (1990).
29. Anson, F. C. & Lingane, J. J. Chemical evidence for oxide films on platinum electrometric electrodes. *J. Am. Chem. Soc.* **79,** 4901–4904 (1957).
30. Smith, A. M., Lee, A. A. & Perkin, S. The electrostatic screening length in concentrated electrolytes increases with concentration. *J. Phys. Chem. Lett.* **7,** 2157–2163 (2016).
31. Gebbie, M. A. *et al.* Long range electrostatic forces in ionic liquids. *Chem. Commun.* (2017).
32. Leroy, S. & Charlaix, E. Hydrodynamic interactions for the measurement of thin film elastic properties. *J. Fluid Mech.* **674,** 389–407 (2011).
33. Elbourne, A. *et al.* Nanostructure of the ionic liquid—graphite stern layer. *ACS Nano* **9,** 7608–7620 (2015).
34. Buchner, F., Forster-Tonigold, K., Bozorgchenani, M., Gross, A. & Jürgen Behm, R. Interaction of a self assembled ionic liquid layer with graphite (0001): a combined experimental and theoretical study. *J. Phys. Chem. Lett.* **7,** 226–233 (2016).
35. Alba-Simionesco, C. *et al.* Effects of confinement on freezing and melting. *J. Phys. Condens. Matter* **18,** R15 (2006).
36. Bhatt, V. D., Gohi, K. & Mishra, A. Thermal energy storage capacity of some phase changing materials and ionic liquids. *Int. J. ChemTech Res.* **2,** 1771e9 (2010).
37. Mahan, G. D. *Many-Particle Physics* (Springer Science and Business Media, 2000).
38. Dibrov, S. M. & Koch, J. K. Crystallographic view of fluidicstructures for room-temperatureionic liquids: 1-butyl-3-methyl-imidazolium hexafluorophosphat. *ActaCryst. C* **62,** o19-o21 (2006).
39. Alam, M. T., Islam, M. M., Okajima, T. & Ohsaka, T. Capacitance measurements in a series of room-temperature ionic liquids at glassy carbon and gold electrode interfaces. *J. Phys. Chem. C* **112,** 16600–16608 (2008).
40. Sweeney, J. *et al.* Control of nanoscale friction on gold in an ionic liquid by a potential-dependent ionic lubricant layer. *Phys. Rev. Lett.* **109,** 155502 (2012).
41. Li, H., Wood, R. J., Rutland, M. W. & Atkin, R. An ionic liquid lubricant enables superlubricity to be switched *in situ* using an electrical potential. *Chem. Commun.* **50,** 4368–4370 (2014).
42. Fajardo, O. Y., Bresme, F., Kornyshev, A. A. & Urbakh, M. Electrotunable lubricity with ionic liquid nanoscale films. *Sci. Rep.* **5,** 7698 (2015).
43. Fajardo, O. Y., Bresme, F., Kornyshev, A. A. & Urbakh, M. Electrotunable friction with ionic liquid lubricants: how important is the molecular structure of the ions? *J. Phys. Chem. Lett.* **6,** 3998–4004 (2015).
44. Kondrat, S., Wu, P., Qiao, R. & Kornyshev, A. A. Accelerating charging dynamics in subnanometre pores. *Nat. Mater.* **13,** 387–393 (2014).
45. Kondrat, S., Georgi, N., Fedorov, M. V. & Kornyshev, A. A. A superionic state in nano-porous double-layer capacitors: insights from Monte Carlo simulations. *Phys. Chem. Chem. Phys.* **13,** 11359–11366 (2011).
46. Kondrat, S. & Kornyshev, A. Superionic state in double-layer capacitors with nanoporous electrodes. *J. Phys. Condens. Matter* **23,** 022201 (2010).

Author contributions

A.S. and L.B. conceived and directed the research. J.C. performed the experiments and analysed the data. A.N., L.B. and A.S., supervised the experiments. V.K., B.C., A.S. and L.B. conducted the theoretical analysis and B.C. performed the molecular simulations. All authors contributed to the scientific discussions and the preparation of the manuscript.

Additional information

Supplementary information is available in the online version of the paper. Reprints and permissions information is available online at www.nature.com/reprints. Publisher's note: Springer Nature remains neutral with regard to jurisdictional claims in published maps and institutional affiliations. Correspondence and requests for materials should be addressed to A.S.

Competing financial interests

The authors declare no competing financial interests.